Graphene Liquid Cells

How to cite:
International Edition: doi.org/10.1002/anie.202007244
German Edition: doi.org/10.1002/ange.202007244

Synthesis of Honeycomb-Structured Beryllium Oxide via Graphene Liquid Cells

Lifen Wang[+], Lei Liu[+], Ji Chen[+], Ali Mohsin, Jung Hwan Yum, Todd W. Hudnall, Christopher W. Bielawski, Tijana Rajh, Xuedong Bai, Shang-Peng Gao,* and Gong Gu**

Abstract: *Using high-resolution transmission electron microscopy and electron energy-loss spectroscopy, we show that beryllium oxide crystallizes in the planar hexagonal structure in a graphene liquid cell by a wet-chemistry approach. These liquid cells can feature van-der-Waals pressures up to 1 GPa, producing a miniaturized high-pressure container for the crystallization in solution. The thickness of as-received crystals is beyond the thermodynamic ultra-thin limit above which the wurtzite phase is energetically more favorable according to the theoretical prediction. The crystallization of the planar phase is ascribed to the near-free-standing condition afforded by the graphene surface. Our calculations show that the energy barrier of the phase transition is responsible for the observed thickness beyond the previously predicted limit. These findings open a new door for exploring aqueous-solution approaches of more metal-oxide semiconductors with exotic phase structures and properties in graphene-encapsulated confined cells.*

Introduction

Graphene, with atomically flat surfaces and the absence of out-of-plane dangling bonds, continues to attract intensive research interest, in particular, as the substrate for van-der-Waals (vdW) epitaxy.[1–9] Due to the thermal and chemical stability of graphene, the epitaxial growth of transition-metal-dichalcogenide thin flakes, metal thin films, flat-lying organic molecules, and II–VI- as well as III–V-compound semiconductor nanowires and few-layer films has been demonstrated successfully on graphene buffer layers or under graphene protection via vapor–solid growth, such as chemical vapor deposition (CVD).[1–9] Nanocrystal growth from solutions encapsulated by top and bottom graphene layers has been investigated as well as leveraging its impermeability and flexibility.[10–12] In contrast to the open environment of the vapor-transport growth in which the precursor species deposit and diffuse on only one layer of graphene, the vdW interaction between the two graphene layers squeezes out most of the liquid, leaving encapsulated solution droplets in a closed liquid cell[13] with a high pressure (up to 1 GPa) imposed on the liquid.[10,14] Exotic crystallization phenomena in this confined space have been reported,[10] and this approach of epitaxial growth of nanocrystals in graphene liquid cells warrants further investigation.

Beryllium oxide (BeO), an excellent electrical insulator with an ultrahigh thermal conductivity, exists in sp^3-hybridized polymorphs such as wurtzite.[15] Early theoretical work concluded that sp^2-hybridized hexagonal BeO (h-BeO) was intrinsically unstable, both energetically and kinetically, and therefore should not exist.[16] Later theoretical studies based on energetic considerations predicted that each cation-anion

[*] L. F. Wang,[+] X. D. Bai
Beijing National Laboratory for Condensed Matter Physics, Institute of Physics, Chinese Academy of Sciences
Beijing 100190 (China)
E-mail: wanglf@iphy.ac.cn
L. Liu,[+] A. Mohsin, G. Gu
Department of Electrical Engineering and Computer Science, University of Tennessee
Knoxville, TN 37996 (USA)
E-mail: ggu1@utk.edu
L. Liu[+]
Department of Materials Science and Engineering, College of Engineering, Peking University
Beijing 100871 (China)
J. Chen[+]
Department of Physics and Astronomy, London Centre for Nanotechnology, Thomas Young Centre, University College London
London WC1H 0AJ (UK)
and
School of physics, Peking University
Beijing 100871 (China)
and
Max Planck Institute for Solid State Research
70569 Stuttgart (Germany)
J. H. Yum, C. W. Bielawski
Center for Multidimensional Carbon Materials (CMCM), Institute for Basic Science (IBS)
Ulsan 44919 (Republic of Korea)
and
Department of Chemistry and Department of Engineering, Ulsan National Institute of Science and Technology (UNIST)
Ulsan 44919 (Republic of Korea)
T. W. Hudnall
Department of Chemistry and Biochemistry, Texas State University
San Marcos, TX 78666 (USA)
T. Rajh
Center for Nanoscale Materials, Argonne National Laboratory
Lemont, IL 60439 (USA)
S. P. Gao
Department of Materials Science, Fudan University
Shanghai 200433 (China)
E-mail: gaosp@fudan.edu.cn
[+] These authors contributed equally to this work.
Supporting information and the ORCID identification number(s) for the author(s) of this article can be found under: https://doi.org/10.1002/anie.202007244.

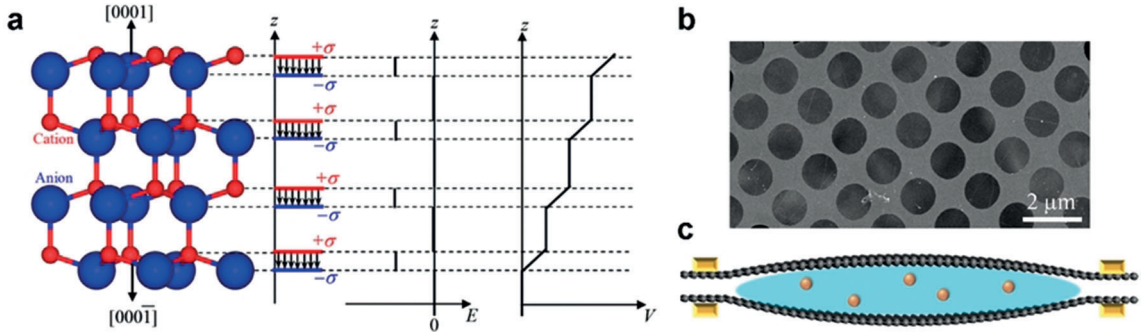

Figure 1. a) Schematic illustration of the polar catastrophe, showing the atomic model of an example polar crystal—the wurtzite structure, and the electrostatic model of the structure along ⟨0001⟩. The electric field *E* gives rise to the divergent potential V, rendering the structure unstable, thus the "catastrophe". b) Representative scanning electron microscope image of one CVD-grown graphene film transferred onto a quantifoil TEM grid by the polymer-free method. c) Schematic of two graphene TEM grids encapsulating a liquid droplet, forming the graphene liquid cell.

bilayer in a free-standing film that would assume polar surfaces in the bulk limit (for example, wurtzite for BeO) should collapse into a planar honeycomb-like structure if and only if the film thickness is below a certain threshold.[17,18] This transformation to the planar structure is deemed a new stabilization mechanism countering the polar field in polar crystals (Figure 1a) in the ultra-thin limit, while a multitude of known mechanisms avert the catastrophic divergence of the electric potential in the bulk and afford stable polar crystals by altering the surface charge densities of the polar surfaces (Figure S1).[19–21] While sp^2-coordinated polymorphs of octet (II–VI, III–V, etc.) compounds, including h-BeO, are predicted to exist in the ultra-thin limit, the experimental synthesis of h-BeO is still missing, and it has remained an intriguing question whether the absence h-BeO demonstrates is due to fundamental limitations or merely technical difficulties in synthesis.

Here, by high-resolution transmission electron microscopy (HRTEM), electron diffraction, and electron energy-loss spectroscopy (EELS) aided by density functional theory (DFT) calculations, we show that BeO crystallizes in a hexagonal structure with h-BN-like basal planes, that is, h-BeO, in liquid cells formed by a top and a bottom graphene sheet. We demonstrate that in graphene-sealed liquid cells, sp^2-bonded h-BeO nanocrystals can exist even beyond the thermodynamically determined layer-count threshold, above which the wurtzite structure (w-BeO) is energetically preferred. The low-loss EELS is consistent with the theoretically calculated plasmon resonance of h-BeO, and the fine structure of the Be K-edge core-loss spectra indicates sp^2 electron configuration. In contrast to previous demonstrations of honeycomb-structured polymorphs of octet compounds,[22,23] where substrate effects have been shown to give rise to a significant deviation of experimental observations from predictions based on free-standing films, the nearly free-standing h-BeO nanocrystals sandwiched between two graphene sheets allow for a glimpse into the intrinsic growth behavior of such polymorphs in the absence of strongly interacting substrates. The discovery calls for further experimental as well as theoretical investigations into sp^2-coordinated polymorphs of octet compounds.

Results and Discussion

Liquid cells are formed by transferring CVD-grown monolayer graphene onto a TEM grid (Figure 1b), exposing it to a small amount of water, covering it with another graphene-dressed TEM grid (Figure 1c), and leaving the assembly to dry on a beryllium sample holder in air to form pockets of liquid trapped between the suspended graphene sheets.[10,11,24,25] HRTEM imaging reveals one type of crystallites exhibiting a distinct in-plane periodicity (Figure 2a as well as Figure S2 and Movie S1 in the Supporting Information), which is a hexagonal lattice with a lattice constant $a = 0.27$ nm, coinciding with the literature value 0.2698 nm for w-BeO.[26] Moreover, Na, Cl, Be, O, and C but no other elements are identified by EELS and energy-dispersive X-ray spectroscopy (Figure S3). As no Na or Cl signatures can be found in regions exhibiting the hexagonal lattice, these crystallites are attributed to BeO that was introduced into the liquid cells via corrosion of the oxide-passivated surface of a beryllium-sample platform by the aqueous solution.[27] Given the nanometer size of the randomly grown crystallites whose ultra-low amount is significantly below the requirements of ex-situ characterizations like synchrotron X-ray diffraction and Raman spectroscopy, the structural phase is fully evaluated by in-situ TEM microscopy and spectroscopy. Figure S2 displays an additional structural survey of crystallites by HRTEM imaging combined with electron-diffraction-pattern measurements which show the homogeneous planer graphitic-like structure of BeO in the graphene cell. The polymorphic phase of the BeO crystallites cannot be determined by imaging alone, since in-plane lattice constants calculated by DFT for h- and w-BeO are 0.2698 and 0.2703 nm, respectively, both close to the measured value (0.27 nm; Table S1).

The BeO crystallites are further examined by EELS, along with w-BeO (Figure 2b) reference samples grown by atomic layer deposition (ALD) on silicon.[28,29] A shift between the low-loss peaks of the graphene-sandwiched crystallites and the w-BeO reference has been observed (Figure 2c). To verify generality, Figure S4 shows the spectra acquired in multiple samples. Consistently, the low-loss peaks arising from valence-electron plasmon resonance are at ≈22 eV and

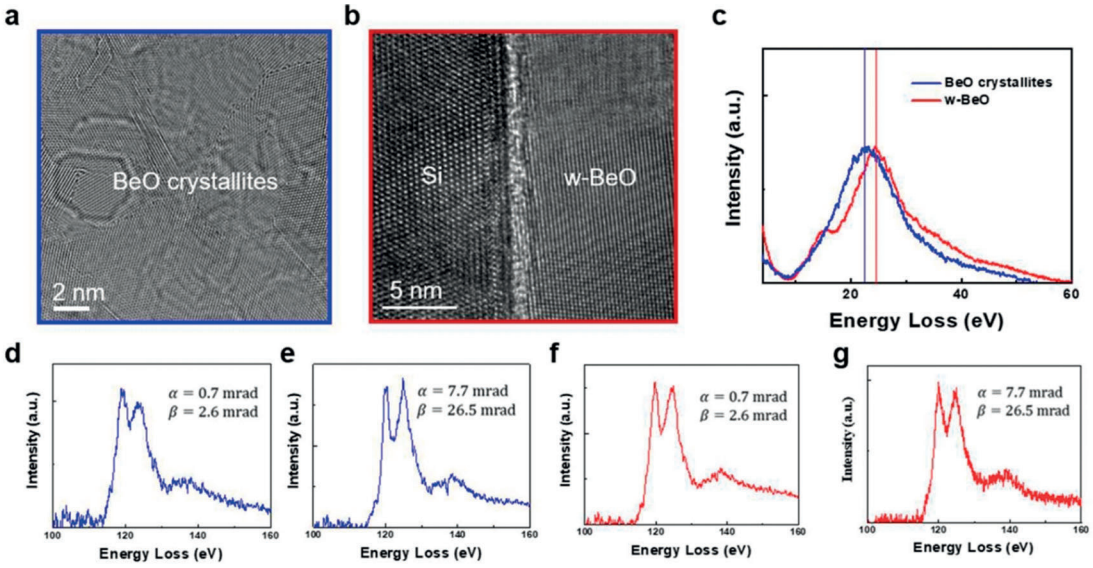

Figure 2. a) Representative high-resolution TEM image of the graphene-sealed BeO nanocrystal. Insets are the fast Fourier transform (FFT) and higher-magnification image of area in dashed blue box. b) TEM image of a w-BeO sample grown on a Si substrate. c) Low-loss spectra of BeO nanocrystals formed in the graphene liquid cell and the w-BeO thin film, acquired at convergence semi-angles $\alpha = 7.7$ mrad and collection semi-angle $\beta = 26.5$ mrad. d)–g) Be K-edge of BeO nanocrystal (blue curve) and w-BeO thin film (red curve) at two sets of (α,β).

≈ 24.1 eV for the crystallites and the w-BeO, respectively, with a ratio of ≈ 0.92. The shift in peak position, along with the difference in shape, once again indicates that the crystallites are a different phase than w-BeO. Qualitatively, the h-BeO (space group: $P6_3/mmc$)/w-BeO unit-cell-volume ratio of 1/0.833 (see lattice constants in Table S1) leads to a loss-peak-energy ratio of 0.91, since the plasmon-resonance energy is proportional to the square root of the valence-electron density. This strong suggestion that the nanocrystals may be h-BeO prompts a close examination of the Be K-edge core-loss spectra of the BeO nanocrystals, again referenced to ALD-grown w-BeO samples, to resolve the angular dependence of the two major peaks (peaks A rising at ≈ 114 eV and B at ≈ 120 eV,[30] Figure 2 d,e) originating from different electronic configurations (sp^2 vs. sp^3).

It is well known that the fine structures of the core-loss spectra, that is, the energy-loss near-edge structures (ELNES), reveal the electronic structures above the Fermi level.[31] Different electronic configurations of h- and w-BeO result in different scattering-angle dependencies in ELNES. Specifically, for reasons to be illustrated after presenting the data, peak A in the Be K-edge is expected to be higher than peak B for very small scattering angles and to intensify and surpass peak B at larger angles for h-BeO. In contrast, for w-BeO, peak A is expected to be stronger than peak B at all scattering angles. However, ultra-small scattering angles on the order of 1 mrad, needed to demonstrate significant differences that rule out any ambiguity, are typically not possible with commercial electron microscopes.[31] This technical challenge has been overcome by using an aperture with 5 μm diameter custom-fabricated by focused ion milling (for details, see the Supporting Information), achieving convergence semi-angles as small as 0.7 mrad. We used a very small convergence semi-angle $\alpha = 0.7$ mrad in conjunction with a more moderate collection semi-angle $\beta = 2.6$ mrad to maintain an adequate signal-to-noise ratio. As expected, the BeO crystallites with graphene encapsulations exhibit a higher peak A than peak B at these small angles (Figure 2 d), but a reversed relative intensity of the two peaks at larger angles $\alpha = 7.7$ mrad and $\beta = 26.5$ mrad (Figure 2 e). In contrast, peak A remains more intense than peak B regardless of the (α,β) combination for the w-BeO sample (Figure 2 f,g). Raw EELS data corresponding to Figure 2 d–g are displayed in Figure S5 to convey the significant difference between the small- and larger-angle spectra for the BeO crystallites as well as the relative intensity variations for w-BeO, which cannot be attributed to a nuance in background removal. More data in Figure S4 g show that peak A is consistently more intense than peak B for w-BeO, while the relative intensity between the two peaks varies for graphene-sandwiched BeO nanocrystals. Furthermore, Be K-edge spectra of BeO crystallites acquired at a series of collection angles reveal that the relative intensity of peak A vs. B reverses around $\beta = 21$ mrad for a fixed $\alpha = 7.7$ mrad, while w-BeO once again exhibits no relative-intensity reversal in the same collection-angle range (Figure 3). The trend is consistent and clear even at these moderate α and β values.

The angular-dependency fine structure of ELNES for BeO crystallites in contrast to the invariant w-BeO reveals the anisotropy features of the hexagonal BeO (h-BeO) nanocrystals. DFT-based calculations find low-loss peak positions for h- and w-BeO at 21.4 and 24.6 eV, respectively (Figure 4 a), closely matching the experimental values of 22 and 24.1 eV. To better mimic the graphene-sealed h-BeO nanocrystals with finite thicknesses, low-loss spectra of stacked h-BeO layers with a graphene cover sheet (Figure S6) exhibit essentially the same low-loss peak position with negligible dependence on h-BeO thickness and choice of

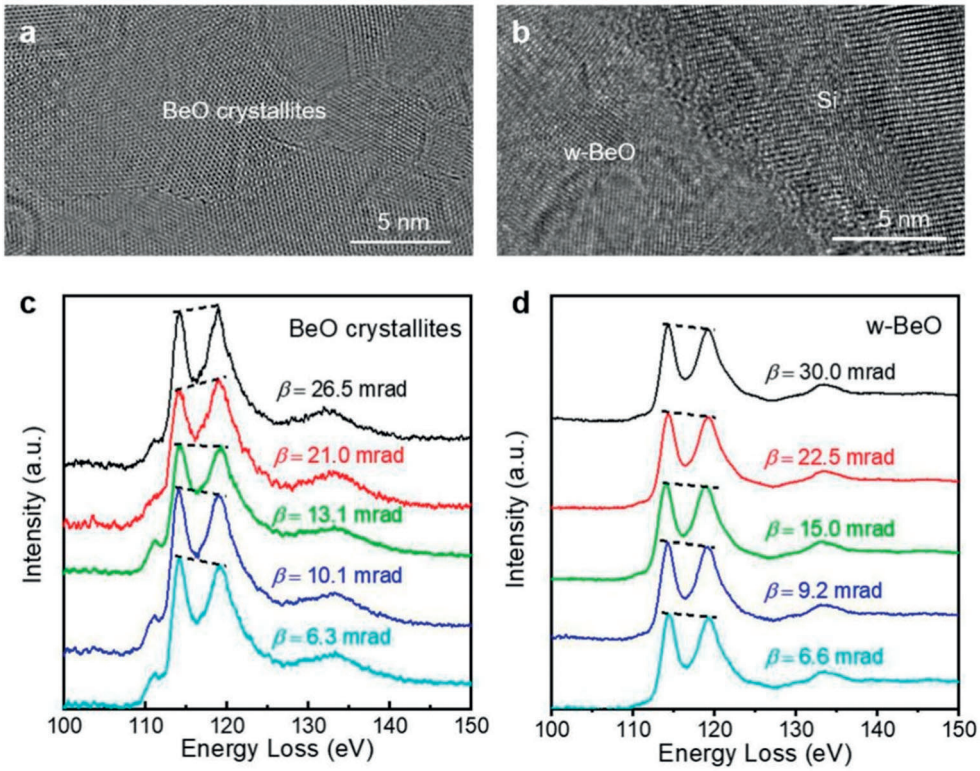

Figure 3. a), b) HRTEM images of BeO nanocrystals and w-BeO, respectively. c), d) Be K-edge acquired at fixed convergence semi-angle $\alpha = 7.7$ and 7.5 mrad and fixed specimen orientation but varying collection semi-angle β in (a) and (b), respectively.

supercell size. We further have performed DFT-based calculations to model the ELNES of both h- and w-BeO. Briefly, under the dipole approximation, the intensity is represented by the square modulus of the position-operator matrix element between the core state (1s) and the unoccupied states (π^*,σ^*), which are explicitly evaluated, with core-hole effects taken into account by employing a specially constructed pseudopotential for the excited atom in a sufficiently large supercell.[32,33] The ELNES dependence on the direction of the momentum transfer manifests the anisotropy of the electron orbitals.[34,35] Due to strong anisotropy between the in-plane sp^2 bonding and the π-bonding formed by p_z orbitals, h-BeO core-loss spectra differ drastically for $\mathbf{q} \parallel \mathbf{c}$ and $\mathbf{q} \perp \mathbf{c}$, where $\mathbf{q}$ is the momentum transfer upon inelastic scattering and $\mathbf{c} \parallel z \parallel [0001]$ (Figure S7). As shown in Figure 4b, with the transition energy from the Be 1s core level to the conduction-band minimum set to 0, the first peak (at ≈ 0.3 eV), arising from the $1s \rightarrow \pi^*$ transition, is intense for $\mathbf{q} \parallel \mathbf{c}$ (π^* being p_z-symmetry-projected states; $\langle 2p_z|\mathbf{r}|1s\rangle \parallel \mathbf{c}$, where $\boldsymbol{r}$ is the position-vector operator) but virtually absent for $\mathbf{q} \perp \mathbf{c}$, while the second major peak (at ≈ 5 eV), attributed to σ^* states ($p_{x,y}$-symmetry-projected), is strong for $\mathbf{q} \perp \mathbf{c}$ and relatively weak for $\mathbf{q} \parallel \mathbf{c}$. On the contrary, the sp^3-bonded w-BeO is less anisotropic, therefore its Be K-edge spectra differ only slightly for $\mathbf{q} \parallel \mathbf{c}$ and $\mathbf{q} \perp \mathbf{c}$.

While the EELS is always an inseparable combination of $\mathbf{q} \parallel \mathbf{c}$, and $\mathbf{q} \perp \mathbf{c}$ responses due to finite convergence and collection angles (2α and 2β, respectively), the difference in anisotropy between the sp^2 and sp^3 electron configurations can be revealed by comparing the trends in which EELS varies as the scattering angle increases for h- and w-BeO (that is, as the relative weight of the $\mathbf{q} \perp \mathbf{c}$ response increases). This is the reason why scattering-angle-dependent EELS measurements have been applied. For the Be K-edge at 80 kV, the angular width of the differential cross-section as a function (approximately Lorentzian) is just below 1 mrad.[31] Therefore, in order for the comparison between EELS acquired at two sets of (α,β) to be unambiguous, the smaller α and β must be close to 1 mrad. As mentioned earlier and described in the Supporting Information, this challenge has been met by employing a home-made aperture, achieving $\alpha = 0.7$ mrad. The Be K-edge spectra shown in Figures 2d–g and 3c,d are consistent with the theory discussed above, indicating that the graphene-sealed nanocrystals are h-BeO. The validity of our theory and calculations has also been checked by comparing the spectra of defect-free and edge-rich regions in h-BeO. As shown in Figure S8, area 1 is almost defect-free, while area 2 contains numerous zigzag edges.

The DFT-based calculations for Be K-edge ELNES of h-BeO with zigzag edges (see Supporting Information) reveals one "pre-peak" at an energy below the two major peaks (Figure S8b). By comparing the EELS spectra of the two areas, the peak rising at 110 eV is appreciable for box 2 (with zigzag edges), while there is a barely visible peak or shoulder rising at ≈ 110 eV for box 1 (defect-free region), consistent with the findings of our calculations. Moreover, for both the defect-free and edge cases, the energy difference between the pre-peak and peak A is ≈ 3 eV, again closely matching the

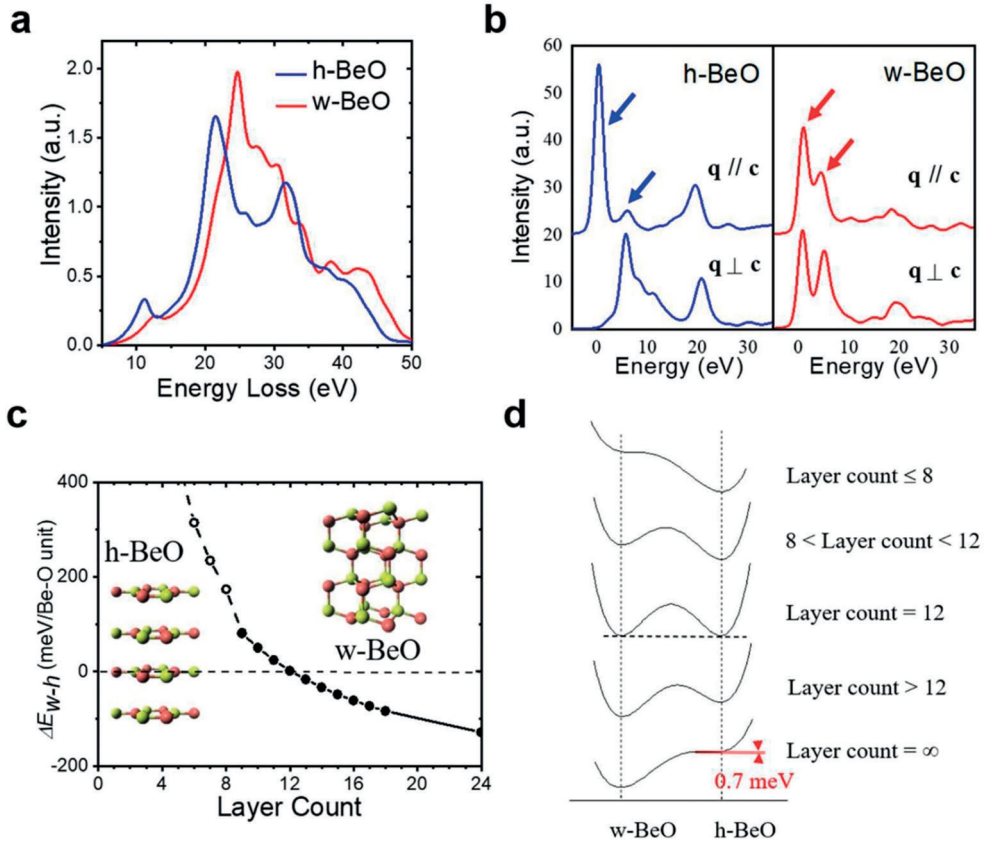

Figure 4. a) Calculated low-loss spectra that reproduce the experimental peak-energy difference between h- and w-BeO. b) Calculated Be K-edges of h- and w-BeO, with the momentum transfer **q** parallel and perpendicular to the lattice vector **c**. c) DFT-calculated total-energy difference, ΔE_{w-h}, between w- and h-BeO slabs vs. layer count. Here, the layer count is defined as the number of h-BeO monolayers for an h-BeO slab, or as the number of BeO bilayers for a w-BeO slab. Insets: Atomic models of w-BeO (right) and an h-BeO monolayer (left). For layer counts ≤ 8, the w-BeO structure collapses into h-BeO upon geometry relaxation (shown as empty circles). d) Schematic depiction of the energy surface in BeO phase space. For layer counts ≤ 8, there is no barrier; for layer counts > 8, a finite barrier exists. The thermodynamic crossover is at a layer count of 12. At the bulk limit, a small yet finite barrier exists.

calculated value of ≈ 3 eV. The confirmation of the defect-state peak by the EELS measurement further shows the reliability of the calculations.

After identifying the graphene-sandwiched BeO nanocrystals as h-BeO, the estimation of the h-BeO thickness and corresponding layer number has been performed by the EELS log-ratio method (see details in the Supporting Information).[31] The h-BeO thickness in Figure 2a is determined to be (8.0 ± 1.6) nm, corresponding to an h-BeO layer count of 28 ± 6, under consideration of the two graphene sheets. Similarly, the layer counts in Figure 3a and four other h-BeO areas are 22 ± 5, 22 ± 5, 18 ± 4, and 22 ± 5, respectively. Thus, the lower bounds of the measured h-BeO layer-count values for these five areas, with the largest possible errors, are 22, 17, 17, 14, and 17, respectively.

The measured layer counts have been compared with the theoretically calculated threshold layer count below which h-BeO is thermodynamically favored. While minimization of the Gibbs free energy is the criterion for stability, it has been shown (see the Supporting Information) that the total energy difference ΔE_{w-h} between w- and h-BeO is a good indicator of the relative stability and that the cross-point $\Delta E_{w-h} = 0$ in Figure 4c reveals that the threshold layer count for the hexagonal–wurtzite transition is 12. The measured layer count of graphene-sandwiched h-BeO can be significantly above the theoretical threshold layer count, even with possible errors of the log-ratio method fully considered (see the Supporting Information).

To reveal why the thermodynamically unfavored h-BeO phase can exist beyond the ultra-thin limit, the kinetic stability of bulk (that is, infinitely thick) h-BeO has been examined by calculating the energy barrier between the w- and h-BeO phases using the solid-state nudged elastic band (SS-NEB) method.[36] The barrier is found to be 0.7 meV per BeO unit cell (Figure S9), too small to stabilize the h-BeO phase. For BeO slabs that are about 10 to 30 layers thick, instead of computationally surveying the energetic landscapes at a high cost, the energy surface has been approximated based on the calculations above. As shown in Figure 4d, for layer counts ≤ 8, the w-BeO structure collapses into h-BeO upon geometry relaxation (see also the empty circles in Figure 4c), indicating the absence of barriers between the two phases. For layer counts > 8, there is a finite barrier, since we can separately optimize the two structures. Our observation of h-BeO crystals beyond the ultra-thin limit indicates that this barrier is significant ($\gg kT = 26$ meV for room temper-

ature) in the thickness range between the thermodynamic threshold (12 layers) and tens of layers. The barrier calculation in the bulk limit (0.7 meV) indicates that this barrier persists although it decreases as the layer count increases. In this scenario, we propose that the energy barrier is responsible for the observed h-BeO layer counts beyond the ultra-thin limit. In other words, the experimentally observed h-BeO is kinetically stabilized by a barrier. Therefore, h-BeO beyond this ultra-thin limit can exist as a metastable polymorph, contrary to a long-held conviction, calling for a re-evaluation of the existence of nonpolar polymorphs of other octet compounds including II–VI and III–V counterparts. The kinetic stabilization revealed here points to the feasibility of layer-by-layer growth of these crystals beyond the ultra-thin limit. Furthermore, the same principle should also allow the growth of van-der-Waals (vdW) heterostructure solids that are widely used in novel physics, a major step forward from mechanical stacking.

We have to point it out that the transition of w-BeO to h-BeO is energetically favorable with layers fewer than the threshold value, while h-BeO beyond the ultrathin limit is kinetically stabilized no matter whether the vdW pressure from graphene sheets is involved in our calculations or not (see the Supporting Information). The role of graphene encapsulation on the formation of h-BeO and the stability of h-BeO beyond the thermodynamic ultra-thin limit is not very clear yet because of the absence of h-BeO crystallization via the aqueous approach in an open cell. One advantage provided by graphene liquid cells is that h-BeO nanocrystals crystallize between the graphene sheets as nearly free-standing layers, because graphene, being a 2D crystal, lacks dangling bonds that would initiate the growth of 3D w-BeO.[1] Furthermore, considering the wafer-scale growth capabilities of graphene, future work on the rational synthesis of nonpolar polymorphs of compound semiconductors, such as ZnO (II–VI compounds) with rich physical and chemical properties, not by high-temperature vapor-transport deposition but via the mild wet-chemistry route with encapsulation of graphene will yield a series of nanocrystals probably holding exotic phase structures, and more importantly, larger crystal size and thus enable ex-situ characterizations such as Raman spectroscopy and X-ray diffraction.

Conclusion

We have demonstrated sp^2-coordinated h-BeO beyond the thermodynamic ultra-thin limit. The h-BeO nanocrystals were formed in the graphene liquid cells and EELS afforded the ideal in-situ experimental means that provide rich information. The h-BeO polymorph was distinguished from w-BeO, which has a nearly identical in-plane lattice, by the low-loss spectrum due to its lower valence-electron density originating from looser packing and by the Be K-edge due to its sp^2 electron configuration. Moreover, the thickness information, revealed by the full spectrum, indicates that as-received h-BeO crystals are significantly thicker than the thermodynamic ultra-thin limit. The barrier between h- and w-BeO phases is proposed to kinetically stabilize the observed h-BeO layer counts beyond the ultra-thin limit as a metastable polymorph.

Considering of the availability of large-area graphene, inspired future work may lead to the rational synthesis of sp^2-coordinated polymorphs of octet compounds, not by high-temperature vapor-phase deposition but via mild wet-chemistry routes. Resulting crystals with a larger area than available in this study will enable more thorough characterizations such as Raman spectroscopy and X-ray diffraction to reveal the rich physics and chemistry of exotic polymorphs that promise novel applications. Our findings open a new avenue towards the solution-phase synthesis of sp^2-coordinated polymorphs of octet compounds in a nearly free-standing form, enabling investigations of their intrinsic structure, properties, and growth behavior in the absence of complicating substrate effects.

Acknowledgements

We thank A. Michaelides for helpful discussions. This work was supported by the National Natural Science Foundation of China (11974001, 11974388, U1932153, 21872172, 51472267, 21773303, 51421002 and 51991344), Program from Chinese Academy of Sciences (Y8K5261B11, ZDYZ2015-1, XDB30000000, XDB33030200, and XDB07030100), DARPA (USA) under grant HR0011-13-2-0016, by NSF (USA) under grants DMR-1410940 and ECCS-1231808, by the Science and Technology Commission of Shanghai Municipality, China (Grant No. 14521100606), by the Beijing Natural Science Foundation (2192022, Z190011), by the National Key R&D Program of China (2019YFA0307801), by the Innovation Program of Shanghai Municipal Education Commission (Grant No. 15ZZ001), by NSF (USA) under CHE-1362140, by the IBS (IBS-R01-019), by the BK21 Plus Program as funded by the Ministry of Education and the National Research Foundation of Korea. Use of the Center for Nanoscale Materials, an Office of Science user facility, was supported by the U.S. Department of Energy, Office of Science, Office of Basic Energy Sciences, under Contract No. DE-AC02-06CH11357. L.W. is grateful for the support from the Youth Innovation Promotion Association of CAS (2020009). Raw data are available upon request.

Conflict of interest

The authors declare no conflict of interest.

Keywords: aqueous-solution synthesis · beryllium oxide · graphene liquid cells · high-resolution transmission electron microscopy · structural phase transition · thermodynamic ultra-thin limit

[1] Y. Kim, S. S. Cruz, K. Lee, B. O. Alawode, C. Choi, Y. Song, J. M. Johnson, C. Heidelberger, W. Kong, S. Choi, K. Qiao, I. Almansouri, E. A. Fitzgerald, J. Kong, A. M. Kolpak, J. Hwang, J. Kim, *Nature* **2017**, *544*, 340 – 343.

[2] Z. Y. Al Balushi, K. Wang, R. K. Ghosh, R. A. Vila, S. M. Eichfeld, J. D. Caldwell, X. Qin, Y. C. Lin, P. A. DeSario, G. Stone, S. Subramanian, D. F. Paul, R. M. Wallace, S. Datta, J. M. Redwing, J. A. Robinson, *Nat. Mater.* **2016**, *15*, 1166 – 1171.
[3] J. Kim, C. Bayram, H. Park, C. W. Cheng, C. Dimitrakopoulos, J. A. Ott, K. B. Reuter, S. W. Bedell, D. K. Sadana, *Nat. Commun.* **2014**, *5*, 4836.
[4] Y. Shi, W. Zhou, A.-Y. Lu, W. Fang, Y. H. Lee, A. L. Hsu, S. M. Kim, K. K. Kim, H. Y. Yang, L. J. Li, J. C. Idrobo, J. Kong, *Nano Lett.* **2012**, *12*, 2784 – 2791.
[5] I. Salzmann, A. Moser, M. Oehzelt, T. Breuer, X. Feng, Z.-Y. Juang, D. Nabok, R. G. Della Valle, S. Duhm, G. Heimel, A. Brillante, E. Venuti, I. Bilotti, C. Christodoulou, J. Frisch, P. Puschnig, C. Draxl, G. Witte, K. Muellen, N. Koch, *ACS Nano* **2012**, *6*, 10874 – 10883.
[6] H.-K. Hong, J. Jo, D. Hwang, J. Lee, N. Y. Kim, S. Son, J. H. Kirn, M.-J. Jin, Y. C. Jun, R. Erni, S. K. Kwak, J. W. Yoo, Z. Lee, *Nano Lett.* **2017**, *17*, 120 – 127.
[7] Y. Alaskar, S. Arafin, D. Wickramaratne, M. A. Zurbuchen, L. He, J. McKay, Q. Lin, M. S. Goorsky, R. K. Lake, K. L. Wang, *Adv. Funct. Mater.* **2014**, *24*, 6629 – 6638.
[8] Z. Lu, X. Sun, M. A. Washington, T. M. Lu, *J. Phys. D* **2018**, *51*, 095301.
[9] A. M. Munshi, H. Weman, *Phys. Status Solidi RRL* **2013**, *7*, 713 – 726.
[10] G. Algara-Siller, O. Lehtinen, F. C. Wang, R. R. Nair, U. Kaiser, H. A. Wu, A. K. Geim, I. V. Grigorieva, *Nature* **2015**, *519*, 443 – 445.
[11] J. M. Yuk, J. Park, P. Ercius, K. Kim, D. J. Hellebusch, M. F. Crommie, J. Y. Lee, A. Zettl, A. P. Alivisatos, *Science* **2012**, *336*, 61 – 64.
[12] C. Wang, Q. Qiao, T. Shokuhfar, R. F. Klie, *Adv. Mater.* **2014**, *26*, 3410 – 3414.
[13] S. J. Haigh, A. Gholinia, R. Jalil, S. Romani, L. Britnell, D. C. Elias, K. S. Novoselov, L. A. Ponomarenko, A. K. Geim, R. Gorbachev, *Nat. Mater.* **2012**, *11*, 764 – 767.
[14] K. S. Vasu, E. Prestat, J. Abraham, J. Dix, R. J. Kashtiban, J. Beheshtian, J. Sloan, P. Carbone, M. Neek-Amal, S. J. Haigh, A. K. Geim, R. R. Nair, *Nat. Commun.* **2016**, *7*, 12126.
[15] D. de Faoite, D. J. Browne, F. R. Chang-Diaz, K. T. Stanton, *J. Mater. Sci.* **2012**, *47*, 4211 – 4235.
[16] A. Continenza, R. M. Wentzcovitch, A. J. Freeman, *Phys. Rev. B* **1990**, *41*, 3540 – 3544.
[17] J. Goniakowski, C. Noguera, L. Giordano, *Phys. Rev. Lett.* **2004**, *93*, 215702.
[18] C. L. Freeman, F. Claeyssens, N. L. Allan, J. H. Harding, *Phys. Rev. Lett.* **2006**, *96*, 066102.
[19] H. Kroemer, *Rev. Mod. Phys.* **2001**, *73*, 783 – 793.
[20] N. Nakagawa, H. Y. Hwang, D. A. Muller, *Nat. Mater.* **2006**, *5*, 204 – 209.
[21] A. Wander, F. Schedin, P. Steadman, A. Norris, R. McGrath, T. S. Turner, G. Thornton, N. M. Harrison, *Phys. Rev. Lett.* **2001**, *86*, 3811 – 3814.
[22] C. Tusche, H. Meyerheim, J. Kirschner, *Phys. Rev. Lett.* **2007**, *99*, 026102.
[23] J. Lee, D. C. Sorescu, X. Deng, *J. Phys. Chem. Lett.* **2016**, *7*, 1335 – 1340.
[24] A. Mohsin, L. Liu, P. Liu, W. Deng, I. N. Ivanov, G. Li, O. E. Dyck, G. Duscher, J. R. Dunlap, K. Xiao, G. Gu, *ACS Nano* **2013**, *7*, 8924 – 8931.
[25] A. Mohsin, N. G. Cross, L. Liu, P. Liu, G. Duscher, G. Gu, *Phys. Status Solidi B* **2017**, *254*, 1700069.
[26] R. M. Hazen, L. W. Finger, *J. Appl. Phys.* **1986**, *59*, 3728 – 3733.
[27] P. D. Miller, W. K. Boyd, **1967**, *AD824446*, http://www.dtic.mil/dtic/tr/fulltext/u2/824446.pdf.
[28] J. H. Yum, T. Akyol, M. Lei, T. Hudnall, G. Bersuker, M. Downer, C. W. Bielawski, J. C. Lee, S. K. Banerjee, *J. Appl. Phys.* **2011**, *109*, 064101.
[29] J. H. Yum, T. Akyol, M. Lei, D. A. Ferrer, T. W. Hudnall, M. Downer, C. W. Bielawski, G. Bersuker, J. C. Lee, S. K. Banerjee, *Thin Solid Films* **2012**, *520*, 3091 – 3095.
[30] C. C. Ahn, O. L. Krivanek, R. P. Burgner, M. M. Disko, P. R. Swann, http://www.eels.info/atlas/beryllium.
[31] R. F. Egerton, *Electron Energy-Loss Spectroscopy in the Electron Microscope*, 3rd ed., Springer, New York, **1996**.
[32] S.-P. Gao, C. J. Pickard, M. C. Payne, J. Zhu, J. Yuan, *Phys. Rev. B* **2008**, *77*, 115122.
[33] S.-P. Gao, C. J. Pickard, A. Perlov, V. Milman, *J. Phys. Condens. Matter* **2009**, *21*, 104203.
[34] N. D. Browning, J. Yuan, L. M. Brown, *Ultramicroscopy* **1991**, *38*, 291 – 298.
[35] S.-P. Gao, *Phys. Status Solidi B* **2010**, *247*, 2190 – 2194.
[36] D. Sheppard, P. Xiao, W. Chemelewski, D. D. Johnson, G. Henkelman, *J. Chem. Phys.* **2012**, *136*, 074103.

Manuscript received: May 19, 2020
Accepted manuscript online: May 28, 2020
Version of record online: ■■ ■■, ■■■■

Research Articles

Graphene Liquid Cells

L. F. Wang,* L. Liu, J. Chen, A. Mohsin, J. H. Yum, T. W. Hudnall, C. W. Bielawski, T. Rajh, X. D. Bai, S. P. Gao,* G. Gu* _____ ■■■■–■■■■

Synthesis of Honeycomb-Structured Beryllium Oxide via Graphene Liquid Cells

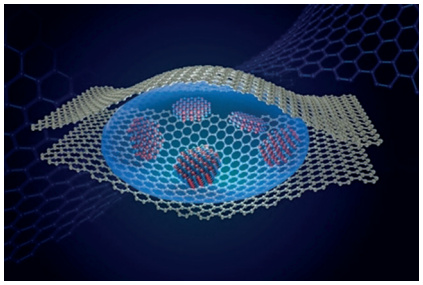

Hexagonal, exceptional: In a graphene liquid cell, beryllium oxide can crystallize in a rare sp^2-coordinated, hexagonal BeO polymorph. The thickness of the crystals produced this way is beyond the thermodynamic ultra-thin limit above which the wurtzite phase is energetically more favorable. Calculations show that the energy barrier of the phase transition is responsible for the observed occurrence of hexagonal layers.